

Vibration and Noise Analysis of Low-Speed High-Torque Permanent Magnet Motor for Forging Equipment Based on PSO

Huoda Hu, Wendong Zhang, and Chaohui Zhao*

School of Electrical, Shanghai Dianji University, Shanghai, China

ABSTRACT: The vibration and noise of a low-speed high-torque permanent magnet motor with a dovetail magnetic isolation device (DMID) structure is analyzed. The motor structure and the main structural parameters of the DMID are introduced, and the radial electromagnetic force wave of the motor is investigated. The notch width, radius, and position of the inner circle of the DMID are selected as design variables, and the constraint conditions are given. The influence of a single parameter on the radial electromagnetic force wave is discussed. The multi-objective optimization of the particle swarm optimization (PSO) algorithm is used to obtain the Pareto relatively optimal solution set that simultaneously satisfies the requirements of low noise, ample output torque, and small torque ripple, and the optimal design scheme is selected. Besides, the harmonic amplitudes of the radial electromagnetic force, motor vibration acceleration, electromagnetic noise, losses, and efficiency are compared and analyzed before and after optimization. Finally, the electromagnetic vibration experiment of a permanent magnet synchronous motor is carried out, and the data shows the feasibility of the above analysis. The results show that the optimal design scheme of the structure parameters of DMID can increase the average output torque, reduce the torque ripple, and effectively reduce the electromagnetic vibration and noise of the motor.

1. INTRODUCTION

With high efficiency, low speed, and high torque advantages [1], low-speed high-torque permanent magnet motors are widely used in forging equipment, medical equipment, and aerospace. As a significant source of industrial noise, effective suppression of vibration noise in forging equipment will ensure manufacturing accuracy, prolong the service life of mechanical equipment, improve labor productivity, and promote the construction of ecological civilizations. Therefore, research on the low noise of low-speed high-torque permanent magnet motors is realistic.

The vibration and noise of permanent magnet motors are closely related to electromagnetic force waves [2, 3]. Electromagnetic force waves on the structure cause electromagnetic vibration. Electromagnetic waves are composed of a superposition of electromagnetic forces that appear as a series of sine waves in space and time. Standard electromagnetic force analysis methods can be divided into Maxwell stress tensor method [4, 5] and virtual work method [5, 6]. The cause of electromagnetic waves can be directly expressed by using a partial differential equation to calculate the magnetic density of the air gap and the Maxwell stress tensor method to analyze them [7]. Electromagnetic force waves strongly correlate with the air gap flux density harmonics. Air gap flux density is necessary for a motor to generate torque. Therefore, electromagnetic vibration can be considered a parasitic effect of motors [8]. As long as the motor is energized and working, electromagnetic vibration will inevitably occur. Besides, mo-

tor vibration and noise can only be optimized by various means. Pang et al. [9] and Zhao et al. [10] optimized air gap flux density distortion rate and power flux density through magnetic pole eccentricity, thus effectively suppressing the vibration and noise of the motor. Tang [11] analyzed harmonic waves of the electromagnetic force of an automotive asynchronous motor in time and space and, based on the study of electromagnetic force waves and the structure modal of the motor, selected a reasonable groove fit to suppress electromagnetic noise. In [12], the torque ripple and noise were reduced by changing the stator and rotor shape. Based on the theoretical analysis of electromagnetic force waves, the influence of different tooth angles on each harmonic amplitude was deduced [13]. Based on the vibration characteristics of a double-sided rotor permanent magnet synchronous motor, Liu et al. [14] proposed the effect of armature tooth offset method on the vibration and noise of the motor. It was verified that the radial electromagnetic force is the primary source of the motor's vibration and noise. The vibration and noise of the permanent magnet synchronous motor will be pronounced when running at low speed. Taking a low-speed high-torque motor as an example, tuning pole-slot coordination and adjusting motor parameters can effectively improve them, and they are suitable for various working conditions [15]. However, using radial electromagnetic force suppression is rare to achieve optimization objectives in vibration and noise analysis of low-speed high torque motors.

Electromagnetic vibration and motor noise are synergistically affected by various factors. Due to the synergistic influence of many factors, many scholars have adopted the multi-objective optimization method to suppress the vibration and

* Corresponding author: Chaohui Zhao (zhaoch@sdju.edu.cn).

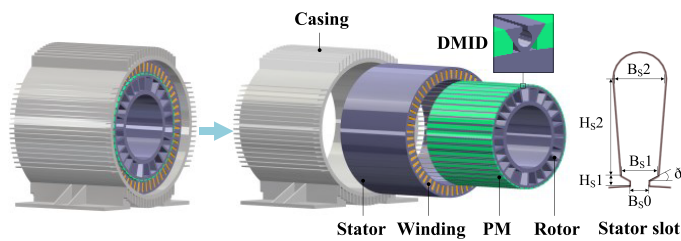


FIGURE 1. Structure diagram of the motor.

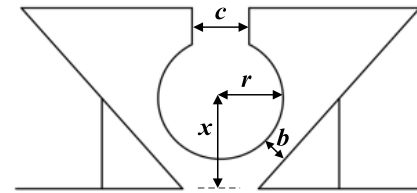


FIGURE 2. Structural diagram of the DMID.

Parameter	Value	Parameter	Value
Rated voltage/V	380	Rated speed/(r/min)	120
Torque/(kN·m)	5.9675	PM material	NdFe35
Poles/Slots	48/54	Iron core material	DW465-50
B_{S0} /mm	3	Stator outer diameter/mm	620
B_{S1} /mm	10.44	Stator inner diameter/mm	500
B_{S2} /mm	15.21	Rotor outer diameter/mm	485
H_{S1} /mm	3	Rotor inner diameter/mm	300
H_{S2} /mm	41	Iron core length/mm	440
$\delta/^\circ$	0.84	Stator slot profile	Pear

TABLE 1. The main structural parameters of the motor.

Symbol	Parameter	Numerical value
c	Notch width of DMID/mm	1.8
r	Inner circle radius of DMID/mm	2
x	Inner circle position of DMID/mm	3
b	Side width of DMID/mm	2.2

TABLE 2. Initial parameters of the DMID.

noise of the motor. In [16], an improved particle swarm optimization (PSO) was selected to iteratively optimize the parameters given the multi-variable and highly nonlinear characteristics of the switched reluctance motor. In [17], sensitivity layering method is used to analyze the multi-objective design variables of hybrid excitation motors. For multiple design parameters, multiple optimization objectives, and the cross-influence between design variables, PSO has been favored by most researchers [18, 19]. Within the range of parameters that meet the constraint conditions, the multi-objective optimization algorithm based on the Pareto optimal solution can simultaneously optimize all the objectives [20].

In this paper, a vibration and noise analysis of a low-speed high-torque permanent magnet motor with a DMID is performed, and the structural characteristics of this motor are described. The radial electromagnetic force waves of the motor are analyzed analytically. The harmonic amplitudes of the even-numbered frequency multiple and the integral multiple of the pole slot, which is the most significant common factor, are obtained. The accuracy of the analysis is verified by finite element simulation. Next, the structural parameters of the DMID are used as design variables, and the constraints are analyzed one by one to observe the effect of a single design variable on the radial electromagnetic force waves. Then, the PSO algorithm is used for multi-objective optimization, and the structural parameters of the DMID are used as design variables. A Pareto, relative optimal solution set, is obtained, which can satisfy the requirements of low motor noise, ample average output torque, and small torque ripple, and the optimal design scheme was selected from it. Finally, the optimization results of the design variables are compared with the initial data to verify that the optimized structure can effectively reduce the electromagnetic vibration and noise of the motor while maintaining the original performance.

2. INTRODUCTION OF MOTOR STRUCTURE

Compared with the traditional low-speed high-torque permanent magnet motor, the tile-shaped permanent magnets in the motor structure, as shown in Figure 1, can increase the pole arc coefficient of the motor to improve the magnetic field distribution in the air gap. At the same time, a dovetail-shaped magnetic isolation device is added between the permanent magnets. On the one hand, this structure can fix tile-shaped permanent magnets well, and it is easy to install permanent magnets. Using this device, while the structure of the stator and rotor remains unchanged, the contact area between the permanent magnet and the air gap is increased; the air gap space is increased; the magnetic flux leakage is reduced; the magnetic field distribution of the air gap is improved; and the device has better electrical performance. On the other hand, the salient pole effect of the motor is used to satisfy the field-weakening operation of the motor and output higher torque, which is suitable for low-speed and high-torque permanent magnet motors used in forging equipment. The main structural parameters of the motors are shown in Table 1.

Figure 2 shows a schematic diagram of the structure of the DMID. The device was shaped like an isosceles trapezoid, with its long side in direct contact with the air gap and its short side connected with the outer diameter of the rotor. The combination of a rectangle and a circle with a radius r forms the inner groove. The rectangle is symmetric along the symmetry axis, with a width of c and a height from the long side of the trapezoid to the circle. To ensure the symmetry of the structural design, the position of the inner circle center only moves up and down, and the position is expressed by the vertical length x from the circle center to the outer diameter of the rotor. An increase in x means that the center of the inner circle of the DMID moves up, as shown by the position of the inner circle of the DMID moving up. At the same time, changes in x and r will affect the

side width b of the DMID, and the initial parameters are shown in Table 2.

3. ANALYSIS OF THE RADIAL ELECTROMAGNETIC FORCE WAVE OF THE LOW-SPEED HIGH-TORQUE PERMANENT MAGNET MOTOR USED IN FORGING EQUIPMENT

Motor noise can be divided into three main types: fluid, mechanical, and electromagnetic ones. Electromagnetic noise is mainly generated by vibration caused by electromagnetic force waves that deform the stator and rotor core surfaces. According to the direction of the air gap magnetic field, the electromagnetic waves can be divided into radial and tangential waves. Since the radial electromagnetic force wave is much larger, this paper mainly uses it as the research object for analysis.

3.1. Analytical Analysis

Because the core magnetic permeability is much greater than the air gap magnetic permeability, the magnetic field lines are perpendicular to the stator and rotor core surfaces. Therefore, the magnetic flux density's radial component $B(\alpha, t)$ is much larger than its tangential component $B_t(\alpha, t)$. According to the Maxwell stress tensor method, the radial electromagnetic force on a unit area or the electromagnetic force waveform at any point in the air gap is:

$$p_r(\alpha, t) = \frac{1}{2\mu_0} [B^2(\alpha, t) - B_t^2(\alpha, t)] \approx \frac{B^2(\alpha, t)}{2\mu_0} \quad (1)$$

where α is the mechanical angle, t the time, and μ_0 the relative air gap magnetic permeability.

The functional relationship between the air gap magnetic flux density $B_\delta(\alpha, t)$ and the magnetomotive force $F(\alpha, t)$ of the unit air gap g is:

$$B_\delta(\alpha, t) = F(\alpha, t)\Lambda_g(\alpha) \quad (2)$$

where $\Lambda_g(\alpha)$ is the relative air gap permeability, and the air gap permeability will change considering the stator slotting effect and rotor saliency effect. Ref. [21] noted that the relative air gap permeability can be approximately expressed as:

$$\Lambda_g(\alpha) = \Lambda_{g0} \left[1 + \sum_m A_m \cos(mZ\alpha) \right] \quad (3)$$

where Λ_{g0} is a constant component of the relative air gap permeability; the air gap harmonic relative permeability A_m is determined by the slot size and air gap length, with $m = 1, 2, 3$; Z is the number of stator slots.

When a sinusoidal wave is used as the power supply, and the current is balanced between phases, the space and time distributions of the magnetomotive force of the stator and the permanent magnet are as follows:

$$F(\alpha, t) = F_s(\alpha, t) + F_r(\alpha, t) \quad (4)$$

$$F_s(\alpha, t) = \sum_v F_v \cos(vp\alpha - S_v wt) \quad (5)$$

$$F_r(\alpha, t) = \sum_\mu F_\mu \cos(\mu p\alpha - \mu wt) \quad (6)$$

where $v = 3k/4 + 1$, $\mu = 2k + 1$, and $k = 0, \pm 1, \pm 2, \pm 3, \dots$; p is the number of pole pairs of the motor; F_v and F_μ are the amplitudes of the vp -th and μp -th harmonics, respectively; $w = 2\pi f$ is the angular frequency of the input current; $S_v = \pm 1$ is the rotation direction of the vp subharmonic wave of the armature magnetic field.

Substituting the above formulas into Equation (1) yields:

$$\begin{aligned} p_r(\alpha, t) &\approx \frac{b^2(\alpha, t)}{2\mu_0} = \frac{1}{2\mu_0} F^2(\alpha, t)\Lambda_g^2(\alpha) \\ &= \frac{\Lambda_g^2(\alpha)F_s^2(\alpha, t)}{2\mu_0} + \frac{\Lambda_g^2(\alpha)F_r^2(\alpha, t)}{2\mu_0} \\ &\quad + \frac{\Lambda_g^2(\alpha)F_s(\alpha, t)F_r(\alpha, t)}{2\mu_0} \end{aligned} \quad (7)$$

The radial electromagnetic force wave is divided into three parts:

$$\text{Stator harmonics: } p_{rss}(\alpha, t) = \frac{1}{2\mu_0} F_s^2(\alpha, t)\Lambda_g^2(\alpha)$$

$$\text{Permanent magnet harmonic: } p_{rrr}(\alpha, t) = \frac{1}{2\mu_0} F_r^2(\alpha, t)$$

$$\Lambda_g^2(\alpha)$$

Stator harmonic and permanent magnet harmonic:

$$p_{rsr}(\alpha, t) = \frac{1}{2\mu_0} F_s(\alpha, t)F_r(\alpha, t)\Lambda_g^2(\alpha)$$

Analytical analysis shows that the harmonic time orders of the radial electromagnetic force wave are mainly concentrated at $2f, 4f$, etc., which are all even multiples of the fundamental frequency f . The spatial order is distributed primarily in the 6th order, 12th order, etc., which is the pole-slot integer multiple of the most significant common factor G .

3.2. Finite Element Analysis

The initial parameters of the DMID in Table 2 were used to carry out the finite element simulation. Figure 3 shows the distribution diagram of the magnetic field lines and the flux density cloud diagram of the motor. The radial electromagnetic force wave is subjected to Fourier decomposition to obtain Figure 4.

When the time order is an even multiple of the fundamental frequency f , and the spatial order is an integral multiple of the most significant common factor G , the harmonic amplitude of the radial electromagnetic force is more extensive, which is consistent with the harmonic amplitude of the radial electromagnetic force obtained in Table 3. Therefore, when the effect of the structural parameters of the DMID on the radial electromagnetic force wave is analyzed, the harmonic amplitudes with even multiples of the fundamental frequency and spatial order that are integer multiples of the most significant common factor of the pole slots should be considered.

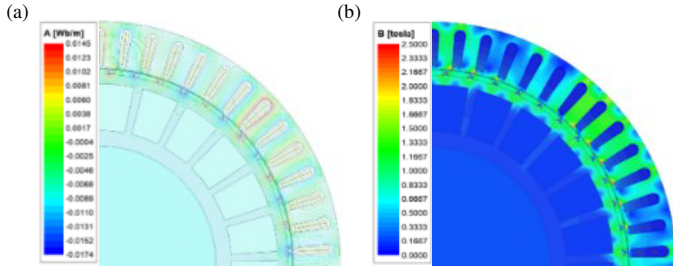


FIGURE 3. Magnetic field lines and magnetic density cloud diagram. (a) Magnetic field lines diagram. (b) Magnetic density cloud diagram.

Source	Amplitude	Time harmonic	Spatial order
Stator	$\sum \sum \frac{F_{\nu 1} F_{\nu 2} \Lambda_{g0}^2}{2\mu_0}$	$(S_{\nu 1} \pm S_{\nu 2}) f$	$(\nu_1 \pm \nu_2) p$
Permanent magnet	$\sum \sum \frac{F_{\mu 1} F_{\mu 2} \Lambda_{g0}^2}{2\mu_0}$	$(\mu_1 \pm \mu_2) f$	$(\mu_1 \pm \mu_2) p$
Stator and permanent magnet	$\sum \sum \frac{F_{\mu} F_{\nu} \Lambda_{g0}^2}{2\mu_0}$	$(\mu \pm S_{\nu}) f$	$(\mu \pm \nu) p$

TABLE 3. Principal components of the radial electromagnetic force wave.

4. OPTIMIZED BASED ON PSO TO REDUCE THE RADIAL ELECTROMAGNETIC FORCE WAVE

It can be seen from the above analysis that the study of motor vibration and noise has focused mainly on the analysis of radial electromagnetic force waves, and a reasonable reduction in the harmonic content of radial electromagnetic force waves is the key to effectively suppress vibration and noise. The design variables are selected from the structural parameters of the DMID to analyze the effect trend of the design variables on the harmonic content in the radial electromagnetic force waves. The harmonic content of the radial electromagnetic force waves is reduced by optimizing the design variable parameters, thereby reducing the motor's electromagnetic force and motor's electromagnetic vibration noise.

4.1. Constraint Conditions and Sensitivity Analysis of the Design Variables

The structure of the DMID is shown in Figure 2. The interior of the DMID is composed of a rectangle and a circle. To ensure the structural integrity of the DMID and limited by the silicon steel sheet production process, the following constraints should be satisfied for the structural parameters of the DMID:

$$\begin{cases} c \leq 2r \\ 0 < x + r < 6 \text{ mm} \\ r < x \\ 0.1 \text{ mm} < r < 2.5 \text{ mm} \\ b \geq 0.5 \text{ mm} \end{cases} \quad (8)$$

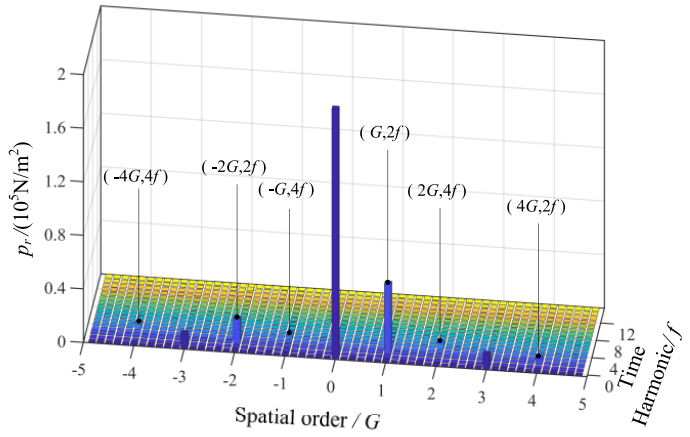


FIGURE 4. Radial electromagnetic force wave diagram.

Symbol	Parameter	Variation range
c	Notch width of DMID/mm	[0.4, 4.0]
r	Inner circle radius of DMID/mm	[0.1, 2.0]
x	Inner circle position of DMID/mm	[2, 4]

TABLE 4. Design variables and variation ranges.

The design variables are the structural parameters of the DMID, including the notch width c of the DMID, radius r of the inner circle of the DMID, and position x of the DMID. Table 4 lists the design variables and variation ranges of the DMID. A sensitivity analysis was performed to observe the effect of the three design variables on the motor noise amplitude A_s , the average value of the output torque T_{avg} , and the output torque ripple T_{ripple} .

The sign of the sensitivity coefficient represents the positive and negative correlations between the design variable and the optimization objective. The greater the absolute value of the sensitivity coefficient is, the more significant the change is in the optimization objective caused by the change in the design variable. In Figure 5, the radius r of the inner circle of DMID has the most significant impact on the noise amplitude A_s and average torque T_{avg} . The value of the position x of the DMID has the most considerable effect on the torque ripple T_{ripple} . The value of the notch width c of the DMID has the most negli-

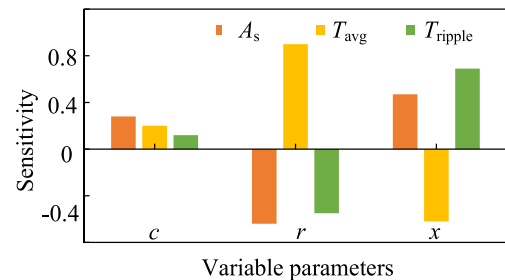


FIGURE 5. Sensitivity of the design variables.

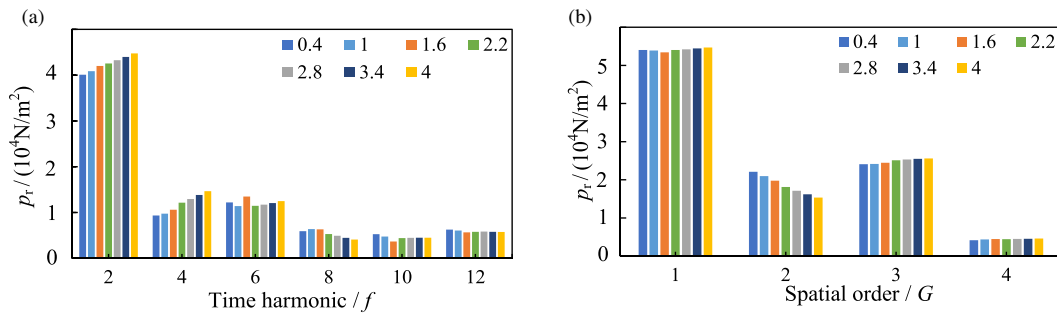


FIGURE 6. Effect of c value on p_r amplitude. (a) Time harmonic distribution. (b) Spatial order distribution.

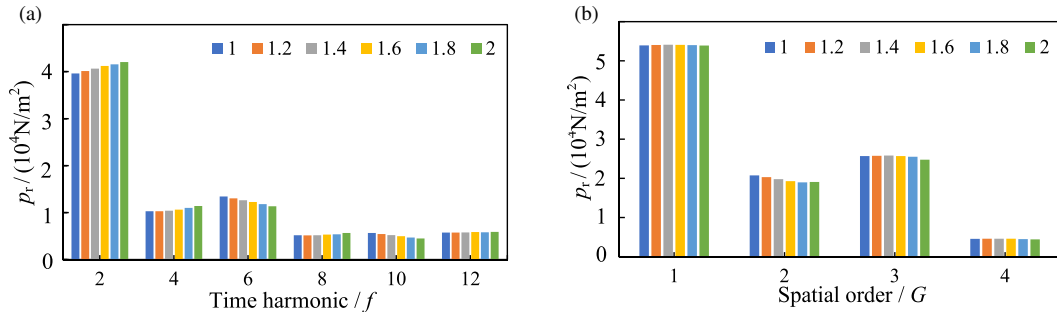


FIGURE 7. Effect of r value on p_r amplitude. (a) Time harmonic distribution. (b) Spatial order distribution.

ble impact on the three optimization objectives. However, to effectively suppress motor vibration and noise, the values of the three design variables must be comprehensively considered. Therefore, the relationship between the structural parameters of the DMID and the radial electromagnetic force wave needs to be further analyzed.

4.2. Effect Analysis of a Single Design Variable on the Radial Electromagnetic Force Wave

The variation pattern of a single structural parameter of DMID on the radial electromagnetic force wave is analyzed through finite element simulation. First, simulation analysis is performed on the notch width c of the DMID. The initial structural parameters of the DMID in Table 2 are kept unchanged, that is, $r = 2 \text{ mm}$ and $x = 3 \text{ mm}$. The value of c ranges from 0.4 mm to 4 mm, and the step is 0.6 mm. Figure 6(a) compares the density amplitude of the even multiples of the fundamental frequency of the radial electromagnetic force harmonics when the value of c is different. As c increases, the amplitudes at $2f$ and $4f$ gradually increase, and the amplitude at $8f$ decreases accordingly. For the amplitude of $6f$, the closer the c is to 1.6 mm, the smaller it is. However, the $6f$ harmonic amplitude is huge when $c = 1.6 \text{ mm}$. The amplitudes at $10f$ and $12f$ have not changed. The minor the c is, the more pronounced the low-order suppression effect is. Figure 6(b) compares the effect of the value of c on the amplitude of the radial electromagnetic force density under different harmonic spatial orders. With c , the $2G$ order harmonic amplitude decreased from 22090.45 N/m^2 to 15361.03 N/m^2 , and the harmonic amplitude fluctuations of the other orders were insignificant. Therefore,

increasing the value of c can effectively suppress the radial electromagnetic force's $2G$ order harmonic amplitude.

Next, the effect of the radius r of the inner circle of the DMID on the radial electromagnetic force wave was observed. When $c = 1.8 \text{ mm}$ and $x = 3 \text{ mm}$, to satisfy the constraint condition in formula (8) that the diameter of the inner circle of the DMID should be no less than the width of the slot, r is selected to vary from 1 mm to 2 mm, and the simulation step size is set to 0.2 mm. According to the data presented in Figure 7(a), the amplitudes of the $2f$, $4f$, $8f$, and $12f$ harmonic waves tend to rise alongside an increase in r . In contrast, the amplitudes of the $6f$ and $10f$ orders gradually decrease. Notably, the $6f$ harmonic wave is most affected by changes in r , with a reduction of 2088.37 N/m^2 observed. Moving on to Figure 7(b), as r continues to increase, the amplitude of the $2G$ order harmonic wave shows a noticeable decreasing trend, while the other order amplitudes remain relatively stable.

Finally, Figure 8 shows the effect of the inner circle position x of the DMID on the radial electromagnetic force wave; at this time, $c = 1.8 \text{ mm}$ and $x = 3 \text{ mm}$. When $x = 2.5 \text{ mm}$, there is a noticeable suppression effect on the $2f$, $4f$, $6f$, $8f$, and $10f$ orders harmonics. As x increases, the G and $3G$ order harmonic amplitudes gradually increase. However, the $2G$ order harmonic wave is the smallest when $x = 3.5 \text{ mm}$. According to the Fourier decomposition of the radial electromagnetic wave in time harmonic, the harmonic amplitude of order $2f$ is the largest. The G order harmonic amplitude is the largest when Fourier decomposition is performed in space. From the aspect of the effect of a single parameter on the radial electromagnetic force wave, when $c = 0.4 \text{ mm}$, $r = 1 \text{ mm}$, and $x = 2.5 \text{ mm}$, the amplitude of the $2f$ order harmonic wave is the smallest;

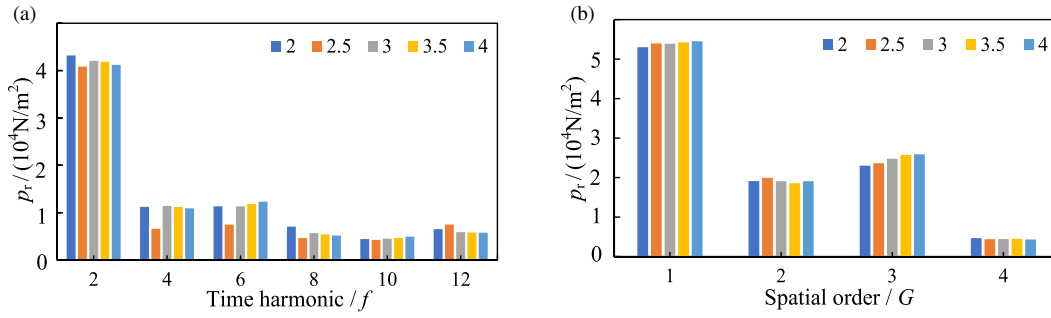


FIGURE 8. Effect of x value on p_r amplitude. (a) Time harmonic distribution. (b) Spatial order distribution.

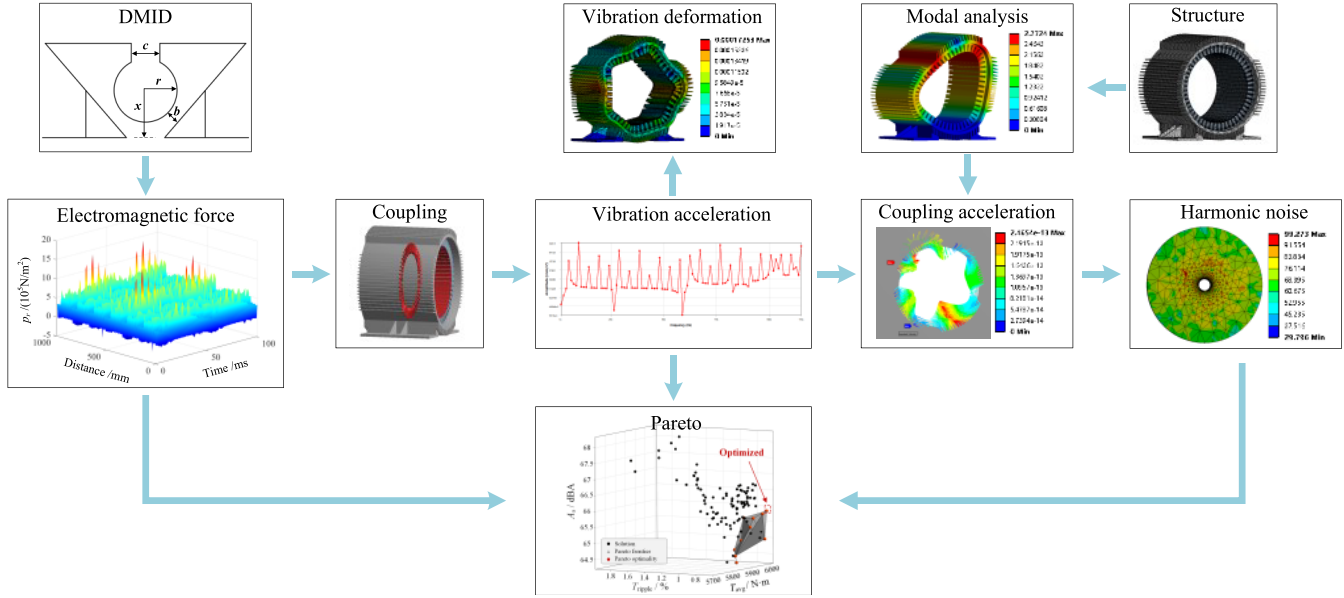


FIGURE 9. Optimization process for electromagnetic vibration and noise.

when $c = 1.6 \text{ mm}$, $r = 2 \text{ mm}$, and $x = 2 \text{ mm}$, the G order harmonic wave has the minimum value.

4.3. Multiobjective Optimization Analysis of Electromagnetic Noise, Output Torque, and Torque Ripple Based on PSO

The selection of design variables under the constraint conditions should meet the optimization objectives of small noise amplitude, ample average torque, and small torque ripple. First, the influence of the design variables on the radial electromagnetic force wave is analyzed one by one. Then, the design variables are examined. Figure 9 shows the flowchart of the optimization simulation for multi-objective optimization.

First, the design variables are selected based on the structural parameters of the DMID; conditional constraints are placed on the design variables; and a sensitivity analysis is performed. The radial electromagnetic force wave of the motor is simulated by the finite element method using Ansys Maxwell. The influence of a single design variable on the radial electromagnetic wave is discussed. Second, the radial electromagnetic force is coupled in the harmonic response to obtain the vibration acceleration, while the vibration deformation of the motor can be observed. Then, the vibration acceleration is connected to

harmonic acoustics to get the corresponding harmonic noise. Finally, the PSO algorithm is used to perform multi-objective optimization through optiSlang. The optimization results of the design variables that simultaneously satisfy the requirements of low motor noise, ample output torque, and low torque ripple are obtained from the Pareto optimal solution set.

The PSO algorithm is widely used because of its ability to converge to the optimal solution quickly. The basic equation of the PSO algorithm is:

$$\begin{cases} V_{id}^{k+1} = \omega V_{id}^k + c_1 r_1 (P_{id}^k - X_{id}^k) + c_2 r_2 (Q_{id}^k - X_{id}^k) \\ X_{id}^{k+1} = X_{id}^k + V_{id}^{k+1} \end{cases} \quad (9)$$

where D is the size of the particle search space; V_{id} is the velocity of the i -th particle in the space; X_{id} is the position of the i -th particle in the space; k is the current iteration number; ω is the inertial weight coefficient; c_1 and c_2 are the local learning factor and global learning factor respectively; r_1 and r_2 are randomly selected in $[0, 1]$; P and Q are regional and global maxima, respectively.

Compared with traditional PSO, the PSO adopted in this paper optimizes the weight coefficients of all examples using the

linear weight reduction method. The inertia weight coefficient ω is linearly reduced from $\omega_{\max} = 0.9$ to $\omega_{\min} = 0.7$; its expression is formula (10). The local learning factor c_1 and global learning factor c_2 are set in asynchronous time-varying mode, and their expression is formula (11). This setting enhances the global search capability in the initial optimization phase and promotes particle convergence to the global optimal solution during the search.

$$\omega = \omega_{\max} - (\omega_{\max} - \omega_{\min}) k / N_{c \max} \quad (10)$$

$$\begin{cases} c_1 = c_{1 \max} - (c_{1 \max} - c_{1 \min}) k / N_{c \max} \\ c_2 = c_{2 \min} + (c_{2 \max} - c_{2 \min}) k / N_{c \max} \end{cases} \quad (11)$$

where $N_{c \max}$ is the maximum number of iterations, set to 10.

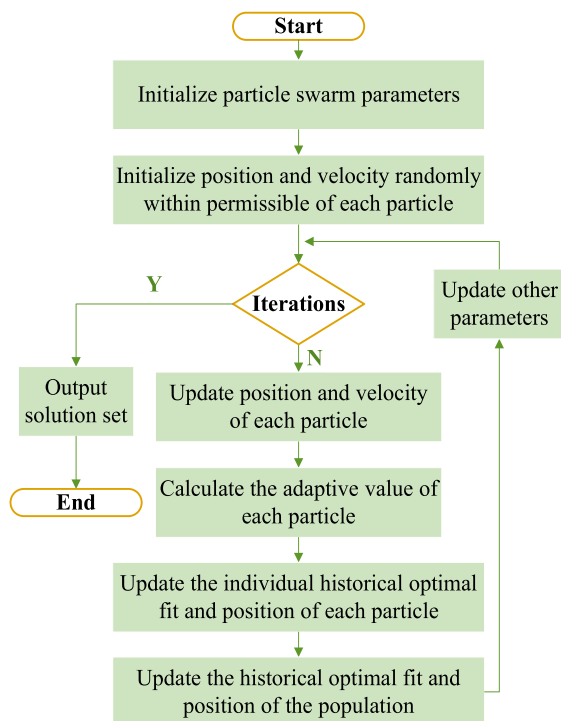


FIGURE 10. Optimization process of the PSO.

Figure 10 is a block diagram of the optimization process. In the multi-objective optimization based on the PSO, the notch width c of the DMID, the radius r , and the position x of the inner circle of the DMID were simultaneously used as the optimization variables. The optimization goals were electromagnetic noise with a radius of 1 meter, the average value of the motor output torque, and the torque ripple. Considering the impact of high-order harmonics on motor noise, the maximum noise amplitude within the range of $24f$ is used as the noise measurement standard in the optimization objective. The starting population size is 20; the population size is 20; the maximum population is 200; and the maximum number of iterations is 10. The specific objective function and constraints conditions are expressed as:

$$f(\varepsilon) = [\min(A_s), \max(T_{\text{avg}}), \min(T_{\text{ripple}})]$$

$$A_s < A_{s0}, T_{\text{avg}} > T_{\text{avg}0}, T_{\text{ripple}} < T_{\text{ripple}0} \quad (12)$$

where $f(\varepsilon)$ is a multi-objective function; ε is the solution to satisfy the objective function. A_{s0} and $T_{\text{ripple}0}$ are the maximum required values of the motor and $T_{\text{avg}0}$ is the minimum.

PSO multi-objective optimization algorithm is used to obtain the solution set that satisfies all the optimization objectives, and Pareto algorithm is used to find the relatively optimal solution set. In essence, Pareto is a state of optimal allocation of resources, which is to achieve further optimization of a specific objective to ensure that other optimization objectives do not deteriorate. Figure 11 shows a three-dimensional diagram of Pareto. The points in the diagram represent the data obtained by multi-objective optimization. The multiple grey planes are collectively called Pareto frontal surface, and the points on the Pareto frontal surface are Pareto's relatively optimal solutions. Table 5 lists the relatively optimal Pareto solution set based on the PSO algorithm and the specific data of points on the Pareto frontal surface in Figure 11.

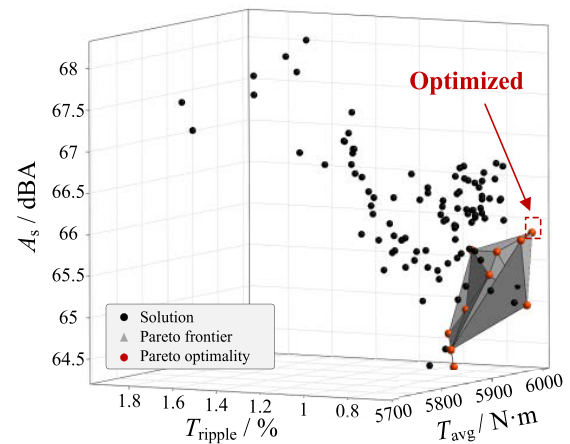


FIGURE 11. Pareto solution.

In Table 5, the maximum value A_s of the A -weighted noise is ranked from low to high. The noise difference of the ten relatively Pareto optimal solutions does not exceed 1.62 dBA. Design Scheme 10 not only had the maximum output torque and lowest torque ripple but also reduced the motor's vibration and noise. Therefore, it was selected as the optimization result.

TABLE 5. Pareto relatively optimal solution set.

ε	c/mm	r/mm	x/mm	A_s/dBA	$T_{\text{avg}}/\text{N}\cdot\text{m}$	$T_{\text{ripple}}/\%$
1	1.24	1.87	2.63	64.20	5979.57	0.97
2	1.26	1.78	2.37	64.43	5966.18	0.95
3	1.01	1.98	2.98	64.59	5985.55	1.01
4	1.48	1.87	2.66	64.88	5992.36	0.94
5	2.58	2.00	2.31	64.99	5984.63	0.65
6	1.47	1.95	2.37	65.32	5987.46	0.83
7	2.22	1.78	2.23	65.59	5996.87	0.81
8	1.66	1.92	2.80	65.59	5998.07	0.93
9	1.83	1.99	2.10	65.81	5956.36	0.61
10	3.61	2.00	2.48	65.82	6011.83	0.69

TABLE 6. Optimization results of the design variables.

Design variable	Value
c/mm	3.6
r/mm	2
x/mm	2.48

TABLE 7. Radial electromagnetic force amplitude comparison.

Losses	Initial	Optimized
Iron core loss/kW	0.2138	0.2064
Copper loss/kW	0.8691	0.8622
Efficiency	0.9414	0.9464

TABLE 8. Simulation conditions of the motor mode.

Casing condition	Value	Stator condition	Value
Material	aluminium alloy	Material	DW465_50
Density/(kg/m ³)	2770	Density/(kg/m ³)	7850
Young's modulus/GPa	71	Young's modulus/GPa	200
Poisson's ratio	0.33	Poisson's ratio	0.3

TABLE 9. Mode vibration shapes and frequencies of each order.


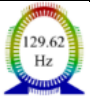

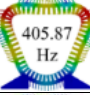


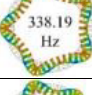
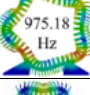


Order	Stator	Stator and casing
2	 42.436 Hz	 129.62 Hz
3	 116.52 Hz	 405.87 Hz
4	 216.75 Hz	 748.81 Hz
5	 338.19 Hz	 975.18 Hz
6	 477.68 Hz	 1535.1 Hz

Table 6 shows the values of the design variables after optimization.

To ensure that the optimization parameters do not lead to motor performance deterioration, the core loss and copper loss of the initial motor and the optimized motor were compared by the finite element method, as shown in Table 7. The optimized motor increased by 0.5% from the efficiency effect, maintaining its performance. Through data comparison, the two data sets have little difference in iron and copper losses and will not cause electromagnetic properties.

5. MODAL ANALYSIS AND VIBRATION AND NOISE VALIDATION

When the electromagnetic force frequency is close to the modal frequency of the motor, it will cause resonance of the motor. Motor resonance can cause large mechanical and structural deformations and dynamic stress and may cause destructive accidents. Therefore, the finite element method is used for motor modal analysis to avoid motor resonance. The literature shows

that the end covers and the rotor have little impact on the vibration of the stator. Therefore, the end covers and the rotor are usually ignored [22, 23].

In modal analysis, finite element analysis is performed on the stator and casing. The lower surface of the motor casing was constrained to simulate the actual working state of the motor. The main motor mode simulation conditions are shown in Table 8. Figure 12 shows the mesh diagram of the modal simulation.

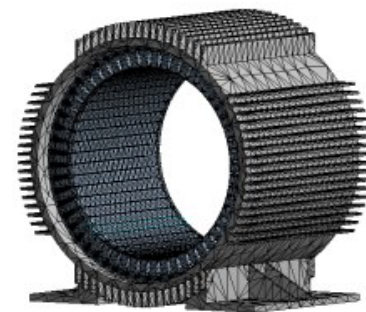
**FIGURE 12.** Modal simulation mesh diagram.

Table 9 shows the vibration modes and frequencies under different modal orders. The corresponding harmonic amplitude increases significantly when the harmonic frequency is similar to the modal frequency. Therefore, when the variation pattern of the harmonic amplitude is analyzed, the motor modal frequency should be considered simultaneously.

In Figure 13(a), the harmonic amplitudes of the $2f$, $4f$, $8f$, and $10f$ orders after optimization are significantly lower than the preoptimization levels, and the suppression effect on the $4f$ order harmonic amplitude is the most obvious, with a reduction of 3190.29 N/m^2 . Regarding spatial order, in Figure 13(b), the $2G$ order harmonic wave decreased the most from the original 19055.47 N/m^2 to 16293.8 N/m^2 or 2761.67 N/m^2 . The optimized design variables are compared with the initial structural parameters of the DMID. Figure 14 compares the harmonic amplitude variations of the radial electromagnetic force wave before and after optimization. Table 10 summarizes the data in Figure 14 and Figure 4. Compared with the initial and opti-

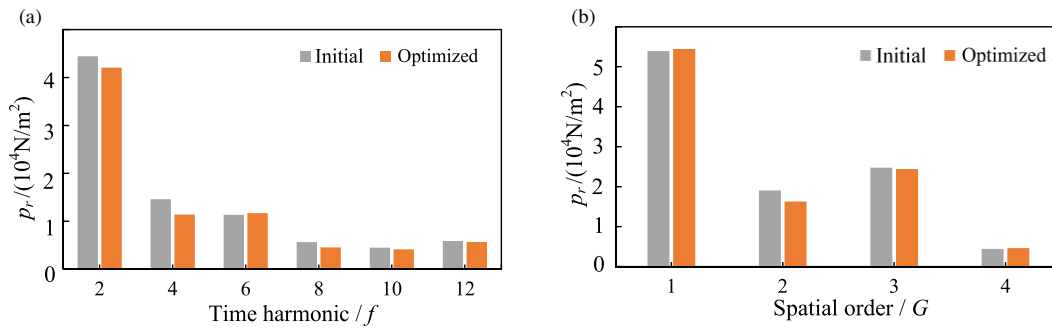


FIGURE 13. Radial electromagnetic force waves comparison. (a) Time harmonic distribution. (b) Spatial order distribution.

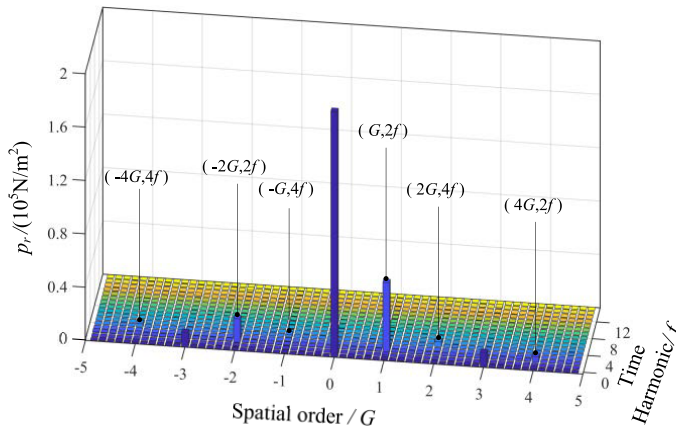


FIGURE 14. Optimized radial electromagnetic force wave diagram.

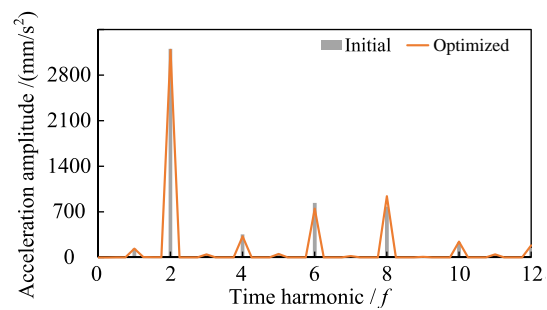


FIGURE 15. Electromagnetic vibration acceleration comparison.

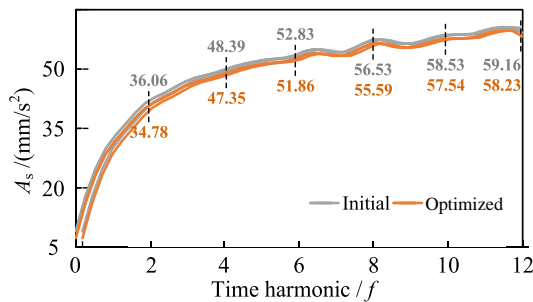


FIGURE 16. A-weighted noise spectra comparison.

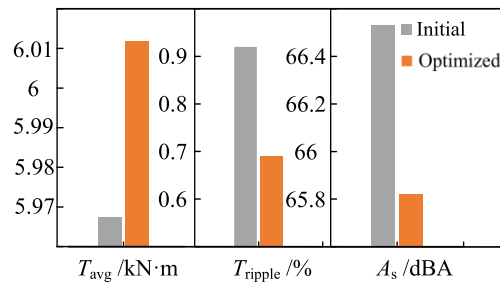


FIGURE 17. Optimization objectives comparison.

TABLE 10. Radial electromagnetic force amplitude comparison.

p_r	Initial/ (10^4N/m^2)	Optimized/ (10^4N/m^2)
$(-4G, 4f)$	0.3369	0.2482
$(-2G, 2f)$	1.8570	1.7372
$(-G, 4f)$	0.2100	0.1606
(G, f)	5.2457	5.2117
$(2G, 4f)$	0.4332	0.3942
$(4G, 2f)$	0.4799	0.4234

mized radial electromagnetic force amplitudes, the harmonics are effectively suppressed when c increases; r increases; and x decreases.

Figure 15 is the comparison of the vibration acceleration spectra. The suppression effect on $4f$ and $6f$ is noticeable,

and the vibration acceleration is reduced by 31.18 mm/s^2 and 87.66 mm/s^2 , respectively. Concerning the modal vibration shapes and frequencies of each order in Table 8, $2f$ is similar to the frequency of the second-order mode of the stator and casing. Therefore, it has more excellent vibration acceleration. At the same time, $8f$ is identical to the third-order mode.

Compared with ordinary noise analysis, A-weighted noise more fully considers the auditory characteristics of the human ear. It is widely used to describe sound sensitivity in different frequency bands. Therefore, performing A-weighted noise analysis on the DMID structure before and after optimization is more accurate, as shown in Figure 16. The maximum noise amplitude within the range of $24f$ was selected for analysis in the multi-objective optimization to optimize the motor's vibration and noise and obtain more reliable data. However, since low

order has a more significant impact on the vibration and noise of the engine, only the data before and after optimization are compared and analyzed within the range of $12f$. On average, the A-weighted noise under the even-frequency order condition decreased by 2%.

Figure 17 shows the comparison before and after the optimization objective. Before and after optimization, the noise within the range of $24f$ was reduced by 1.1%, the average value of the output torque increased by 44.33 N·m, and the torque ripple decreased from 0.92% to 0.69%. Based on the above verification analysis, optimizing the notch width c , inner circle radius r , and position x of the DMID can effectively suppress the motor's electromagnetic vibration and noise by improving motor performance.

6. EXPERIMENTAL ANALYSIS OF ELECTROMAGNETIC VIBRATION NOISE

A permanent magnet synchronous motor is tested by vibration experiment to verify the larger amplitude of vibration noise at even frequency multiples. Figure 18 shows the motor's electromagnetic vibration test platform, which consists of an SCADAS multi-channel data collector, PB-type single-axis magnetic particle brake, KTC800A torque controller, and vibration acceleration sensors.

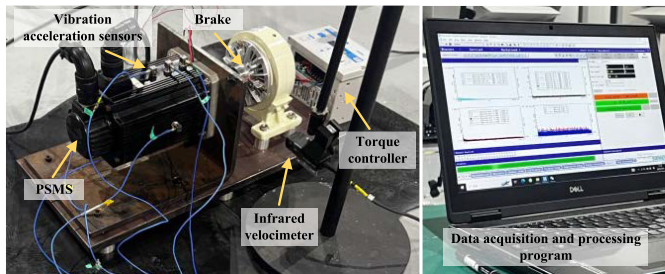


FIGURE 18. Electromagnetic vibration test platform.

Figure 19 is the amplitude of vibration acceleration obtained from the test platform. The vibration acceleration amplitude is the maximum at $4f$, and the vibration amplitude is the local maximum at $2f$, $8f$, $10f$, and $12f$. Therefore, the above analysis can be verified, and vibration noise can be effectively reduced by suppressing the radial electromagnetic force amplitude of the even-numbered frequency multiple.

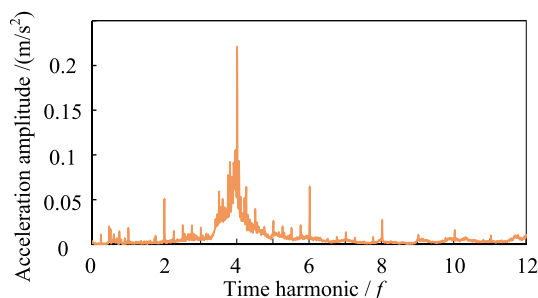


FIGURE 19. Electromagnetic vibration acceleration comparison.

7. CONCLUSIONS

In this paper, a vibration and noise analysis of the low-speed high-torque permanent magnet motor used in forging equipment was performed. The distribution of the radial electromagnetic force wave was analyzed for the low-speed high-torque permanent magnet motor with a DMID, and the radial electromagnetic force wave was obtained through finite element simulation. A comparison of the simulation results and analysis verified the rationality of the analysis. Next, under the constraint condition, the effect patterns of the structural parameters of the DMID on the time-harmonic and spatial order amplitudes of the radial electromagnetic force were analyzed sequentially. Based on the PSO, multi-objective optimization of the noise, average output torque, and torque ripple were performed by using the notch width of the DMID and the radius and position of the inner circle of the DMID as design variables. The Pareto, a relatively optimal solution set, selected the solution with the maximum output torque, relatively small torque ripple, and effective motor vibration and noise reduction as the final optimization scheme. Finally, based on the frequency of each order modal frequency of the motor, the electromagnetic vibration and noise before and after optimization were compared and analyzed, and the following conclusions were obtained:

(1) The radial electromagnetic force waves of the low-speed high-torque permanent magnet motor mainly comprise stator harmonics, permanent magnet harmonics, and the joint action of stator and permanent magnet harmonics. From the perspective of time distribution, the harmonic amplitude of the even frequency multiple is significantly larger than that of the odd frequency multiple. From the standpoint of spatial distribution, the integer multiple harmonic amplitude of the most significant common factor of the pole and slot is significantly larger.

(2) Based on PSO, the three objectives of low electromagnetic noise, considerable average value of the output torque, and small torque ripple are simultaneously optimized. The optimal optimization design scheme is selected from the Pareto relative optimal solution set. Based on the modal analysis, the data of the DMID before and after optimization are compared. When the average torque increases by 44.33 N·m, and the torque ripple decreases by 0.23%, from the harmonic amplitude, the $4f$ order harmonic amplitude decreases by 3190.29 N/m^2 , and the $2G$ order harmonic amplitude decreases by 2761.67 N/m^2 . From the perspective of vibration acceleration, the $4f$ and $6f$ orders decrease by 31.18 mm/s^2 and 87.66 mm/s^2 , respectively. From the noise point of view, the average noise within the 12-order frequency is reduced by 2%, and the maximum noise within the 24-order frequency is decreased by 1.1%.

REFERENCES

- [1] Qi, Z. H., "Design and analysis of the structure and cooling system of hybrid double-rotor low-speed high-torque motor," Ph.D. dissertation, Shenyang University of Technology, Shenyang, China, 2023.
- [2] Deng, X. H., S. W. Zhao, X. Y. Yang, *et al.*, "Magnetic permeance phase bias technology and its application in compressor electromagnetic noise suppression," *Proceedings of the CSEE*, 1–12, 2024.

- [3] Sun, H. S., "Analysis of vibration modal factors and structural resonance control of automobile steering motor," Ph.D. dissertation, Shenyang University of Technology, Shenyang, China, 2023.
- [4] Wang, X. Y., X. Y. He, and P. Gao, "Research on electromagnetic vibration and noise reduction method of V type magnet rotor permanent magnet motor electric vehicles," *Proceedings of the CSEE*, Vol. 39, No. 16, 4919–4926+4994, 2019.
- [5] Zhang, T., G. L. Li, R. Zhou, *et al.*, "Modeling of torque of magnetoresistive spherical motor using virtual work method," *Advanced Technology of Electrical Engineering and Energy*, Vol. 43, No. 1, 24–31, 2024.
- [6] Liu, J., J. Bai, P. Zheng, S. Zhang, M. Wang, and Z. Yin, "Torque analysis of magnetic-field-modulated double-rotor machines with virtual work method," in *2018 21st International Conference on Electrical Machines and Systems (ICEMS)*, 1885–1889, Jeju, Korea (South), 2018.
- [7] Xing, Z., X. Wang, W. Zhao, and G. Ma, "Calculation of electromagnetic force waves and analysis of stator vibration characteristics of surface mount permanent magnet synchronous motor," *Proceedings of the CSEE*, Vol. 41, No. 14, 5004–5013, 2021.
- [8] Lan, H., "Research on electromagnetic force waves and electromagnetic vibration of PMSMs," Ph.D. dissertation, Harbin Institute of Technology, Harbin, China, 2019.
- [9] Pang, L., Q.-L. Yang, C.-H. Zhao, H.-B. Shen, W.-D. Zhang, and H.-H. Qin, "Vibration and noise study of hybrid excitation synchronous motors with magnetic pole eccentricity and tangential magnetizing parallel structure," *Noise and Vibration Control*, Vol. 43, No. 3, 47–52, 2023.
- [10] Zhao, G. X., Y. Zhang, H. Y. Ge, Y. Liu, and B. D. Bai, "Prediction of flux density distribution in permanent magnet motor with eccentric magnetic pole," *Electric Machines and Control*, Vol. 24, No. 6, 24–32, 2020.
- [11] Tang, Y. C., "Asynchronous motor vibration and noise of study on electromagnetic," Ph.D. dissertation, Southwest Jiaotong University, Chengdu, China, 2022.
- [12] Yang, I.-J., S.-H. Lee, K.-B. Lee, J. Lee, W.-H. Kim, and I.-S. Jang, "A process to reduce the electromagnetic vibration by reducing the spatial harmonics of air gap magnetic flux density," *IEEE Transactions on Magnetics*, Vol. 57, No. 2, 8103006, 2021.
- [13] Li, Y., S. Li, J. Zhou, and L. Li, "Weakening approach of the vibration and noise based on the stator tooth chamfering in PMSM with similar number of poles and slots," *Transactions of China Electrotechnical Society*, Vol. 30, No. 6, 45–52, 2015.
- [14] Liu, K., B. Y. Zhang, and G. H. Feng, "Research on electromagnetic vibration and noise characteristics of dual sided rotor permanent magnet synchronous motor based on armature off-set approach," *Transactions of China Electrotechnical Society*, Vol. 36, No. S1, 95–106, 2021.
- [15] Wang, B., Q. Zhang, T. Wu, H. Liu, C. Rong, J. Yu, and D. Zhang, "Optimization of permanent magnet synchronous motor for industrial ceiling fans based on differential evolutionary algorithm," in *2023 IEEE 6th Student Conference on Electric Machines and Systems (SCEMS)*, 1–5, Huzhou, China, 2023.
- [16] Li, F., W. Hua, M. Tong, G. Zhao, and M. Cheng, "Nine-phase flux-switching permanent magnet brushless machine for low-speed and high-torque applications," *IEEE Transactions on Magnetics*, Vol. 51, No. 3, 8700204, 2015.
- [17] Wang, X., Y. Fan, C. Yang, Z. Wu, and C. H. T. Lee, "Multi-objective optimization framework of a radial-axial hybrid excitation machine for electric vehicles," *IEEE Transactions on Vehicular Technology*, Vol. 72, No. 2, 1638–1648, 2023.
- [18] Ma, C. and L. Qu, "Multiobjective optimization of switched reluctance motors based on design of experiments and particle swarm optimization," *IEEE Transactions on Energy Conversion*, Vol. 30, No. 3, 1144–1153, 2015.
- [19] Zhang, P., G. Y. Sizov, D. M. Ionel, and N. A. O. Demerdash, "Establishing the relative merits of interior and spoke-type permanent-magnet machines with ferrite or NdFeB through systematic design optimization," *IEEE Transactions on Industry Applications*, Vol. 51, No. 4, 2940–2948, 2015.
- [20] Sindhya, K., A. Manninen, K. Miettinen, and J. Pippuri, "Design of a permanent magnet synchronous generator using interactive multiobjective optimization," *IEEE Transactions on Industrial Electronics*, Vol. 64, No. 12, 9776–9783, 2017.
- [21] Gieras, J. F. and C. Wang, "Noise of polyphase electric motors," Taylor & Francis Group, 2016.
- [22] Deng, W. and S. Zuo, "Electromagnetic vibration and noise of the permanent-magnet synchronous motors for electric vehicles: An overview," *IEEE Transactions on Transportation Electrification*, Vol. 5, No. 1, 59–70, 2019.
- [23] Fang, H., D. Li, R. Qu, and P. Yan, "Modulation effect of slotted structure on vibration response in electrical machines," *IEEE Transactions on Industrial Electronics*, Vol. 66, No. 4, 2998–3007, 2019.